



# The Kiloparsec-scale Neutral Atomic Carbon Outflow in the Nearby Type 2 Seyfert Galaxy NGC 1068: Evidence for Negative AGN Feedback

Toshiki Saito<sup>1,2</sup> , Shuro Takano<sup>1</sup> , Nanase Harada<sup>2,3</sup> , Taku Nakajima<sup>4</sup> , Eva Schinnerer<sup>5</sup> , Daizhong Liu<sup>6</sup> , Akio Taniguchi<sup>7</sup> , Takuma Izumi<sup>2,3</sup> , Yumi Watanabe<sup>8</sup>, Kazuharu Bamba<sup>8</sup> , Eric Herbst<sup>9</sup> , Kotaro Kohno<sup>10,11</sup> , Yuri Nishimura<sup>2,10</sup> , Sophia Stuber<sup>5</sup> , Yoichi Tamura<sup>7</sup> , and Tomoka Tosaki<sup>12</sup>

<sup>1</sup> Department of Physics, General Studies, College of Engineering, Nihon University, 1 Nakagawara, Tokusada, Tamuramachi, Koriyama, Fukushima, 963-8642, Japan; [toshiki.saito@nao.ac.jp](mailto:toshiki.saito@nao.ac.jp), [saito.toshiki@nihon-u.ac.jp](mailto:saito.toshiki@nihon-u.ac.jp)

<sup>2</sup> National Astronomical Observatory of Japan, 2-21-1 Osawa, Mitaka, Tokyo, 181-8588, Japan

<sup>3</sup> Department of Astronomy, School of Science, The Graduate University for Advanced Studies (SOKENDAI), 2-21-1 Osawa, Mitaka, Tokyo, 181-1855 Japan

<sup>4</sup> Institute for Space-Earth Environmental Research, Nagoya University, Furo-cho, Chikusa-ku, Nagoya, Aichi 464-8601, Japan

<sup>5</sup> Max-Planck-Institut für Astronomie, Königstuhl 17, D-69117, Heidelberg, Germany

<sup>6</sup> Max-Planck-Institut für Extraterrestrische Physik (MPE), Giessenbachstr. 1, D-85748 Garching, Germany

<sup>7</sup> Division of Particle and Astrophysical Science, Graduate School of Science, Nagoya University, Furocho, Chikusa-ku, Nagoya, Aichi 464-8602, Japan

<sup>8</sup> Division of Human Support System, Faculty of Symbiotic Systems Science, Fukushima University, Fukushima 960-1296, Japan

<sup>9</sup> Departments of Chemistry and Astronomy, University of Virginia, Charlottesville, VA 22904, USA

<sup>10</sup> Institute of Astronomy, School of Science, The University of Tokyo, 2-21-1, Osawa, Mitaka, Tokyo 181-0015, Japan

<sup>11</sup> Research Center for the Early Universe, School of Science, The University of Tokyo, 7-3-1 Hongo, Bunkyo-ku, Tokyo 113-0033, Japan

<sup>12</sup> Joetsu University of Education, Yamayashiki-machi, Joetsu, Niigata 943-8512, Japan

Received 2021 December 17; revised 2022 February 23; accepted 2022 March 1; published 2022 March 15

## Abstract

Active galactic nucleus (AGN) feedback is postulated as a key mechanism for regulating star formation within galaxies. Studying the physical properties of the outflowing gas from AGNs is thus crucial for understanding the coevolution of galaxies and supermassive black holes. Here we report 55 pc resolution ALMA neutral atomic carbon [C I]  $^3P_1-^3P_0$  observations toward the central 1 kpc of the nearby Type 2 Seyfert galaxy NGC 1068, supplemented by 55 pc resolution CO( $J=1-0$ ) observations. We find that [C I] emission within the central kiloparsec is strongly enhanced by a factor of  $>5$  compared to the typical [C I]/CO intensity ratio of  $\sim 0.2$  for nearby starburst galaxies (in units of brightness temperature). The most [C I]-enhanced gas (ratio  $> 1$ ) exhibits a kiloparsec-scale elongated structure centered at the AGN that matches the known biconical ionized gas outflow entraining molecular gas in the disk. A truncated, decelerating bicone model explains well the kinematics of the elongated structure, indicating that the [C I] enhancement is predominantly driven by the interaction between the ISM in the disk and the highly inclined ionized gas outflow (which is likely driven by the radio jet). Our results strongly favor the “CO dissociation scenario” rather than the “in situ C formation” one, which prefers a perfect bicone geometry. We suggest that the high-[C I]/CO intensity ratio gas in NGC 1068 directly traces ISM in the disk that is currently dissociated and entrained by the jet and the outflow, i.e., the “negative” effect of the AGN feedback.

*Unified Astronomy Thesaurus concepts:* Active galactic nuclei (16); Galaxy nuclei (609); Galaxy winds (626); Interstellar atomic gas (833); Interstellar phases (850); Molecular gas (1073); Seyfert galaxies (1447)

## 1. Introduction

Galactic outflows are a key phenomenon and feedback mechanism in galaxies regulating star formation and galaxy quenching. These can be driven by active star formation, accreting supermassive black holes (active galactic nuclei, AGNs), or both at the centers of galaxies. Cold gas outflows especially are a subject of great interest, as they contain the raw material from which stars are formed, and thus potentially destine the evolution of galaxies (see the review by Veilleux et al. 2020). AGN-driven outflows affecting the surrounding interstellar medium (ISM), i.e., AGN feedback, are considered to play a critical role in the coevolution of supermassive black holes and their host galaxies (e.g., Magorrian et al. 1998; Costa et al. 2014).

However, there are two long-standing, contradictory paradigms regarding the effect of AGN feedback: “positive” feedback and “negative” feedback. In the positive-feedback scenario, AGN outflows or jets induce star formation through the interaction and compression of the surrounding materials (e.g., van Breugel & Dey 1993; Silk 2013). Negative feedback, in contrast, suppresses or even inhibits star formation by sweeping up and heating ISM (e.g., Croft et al. 2006; Sturm et al. 2011). Understanding the exact AGN feedback mechanism and its role in galaxy evolution is thus one of the challenges of modern astrophysics.

In this Letter, we present tangible evidence for ongoing negative feedback in the nearby ( $\sim 13.97$  Mpc; Anand et al. 2021) Type 2 Seyfert galaxy NGC 1068 using high-quality ALMA [C I]  $^3P_1-^3P_0$  (hereafter [C I](1-0)) and CO(1-0) data sets. The outflow and the jet of NGC 1068 are well studied because of their close distance and apparent brightness (e.g., Wilson & Ulvestad 1983; Das et al. 2006; Barbosa et al. 2014; García-Burillo et al. 2014, 2019). Based on our findings as well as multiwavelength studies in the literature, we provide a



Original content from this work may be used under the terms of the [Creative Commons Attribution 4.0 licence](https://creativecommons.org/licenses/by/4.0/). Any further distribution of this work must maintain attribution to the author(s) and the title of the work, journal citation and DOI.

plausible explanation of what drives and how significant is the negative effect of the AGN feedback in NGC 1068.

## 2. Observations and Data Processing

*ALMA data summary:* We observed [C I](1–0) at  $\nu_{\text{rest}} = 492.16065$  GHz using Band 8 and CO(1–0) at  $\nu_{\text{rest}} = 115.27120$  GHz using Band 3 (2017.1.00586.S, S. Takano et al., in preparation; and 2018.1.01684.S, T. Tosaki et al., in preparation) using the ALMA 12 m array and the ACA 7 m array. The 12 m + 7 m [C I](1–0) data (CO(1–0) data) achieved a spatial resolution of  $\sim 0''.7$  ( $\sim 0''.4$ ) and a maximum recoverable scale (MRS) of  $\sim 14''$  ( $\sim 59''$ ) with a native spectral resolution of  $1.19 \text{ km s}^{-1}$  ( $0.74 \text{ km s}^{-1}$ ). The achieved noise rms levels are  $\sim 0.05$  K for the [C I](1–0) cube and  $\sim 0.35$  K for the CO(1–0) cube.

As the [C I](1–0) field of view (FoV) ( $\sim 16''$ ) is much smaller than the CO(1–0) FoV ( $\sim 71''$ ), we targeted [C I] line emission from three representative positions of NGC 1068, i.e., the circumnuclear disk (CND) and the bar (FoV-1) and the southern and eastern parts of the starburst ring (FoV-2 and FoV-3). In this Letter, we focus on the central 1 kpc FoV-1, and the details of the remaining data will be presented by S. Takano et al. (in preparation).

Both our [C I](1–0) and CO data might suffer from the interferometric spatial filtering effect. As the MRS of the [C I](1–0) data is smaller than that of the CO data, the [C I]/CO line ratios presented in this Letter can be regarded as the lower limits. Thus, this does not affect our discussion and conclusion on the extremely high-[C I]/CO-ratio gas. In addition, the missing flux effect might be minor or negligible, as the spatial structures of the [C I]/CO line ratio gas are basically smaller than the MRS of the [C I](1–0) data ( $\sim 14''$ ).

*Imaging:* We performed the observatory-delivered calibration with minor manual data flagging (e.g., baseline and time flagging). Then, we reconstructed images using the PHANGS-ALMA imaging pipeline (Leroy et al. 2021). During the imaging process of our data, only single-scale CLEAN was employed (i.e., no multiscale CLEAN). Aside from this, we followed the recommended standard setups (see Leroy et al. 2021 for more details).

*Postprocessing:* After imaging, the clean products are corrected for primary beam, convolved to a round  $0''.8$  beam ( $\sim 55$  pc), and regridded to  $0''.2$  pixel size. Then, moment maps are extracted from the data cubes using the imaging pipeline. As we focus on line ratios in this study, high signal-to-noise ratio (S/N) in both lines is required. Therefore, we use the “strictly masked” moment map, which is based on an S/N mask (see Leroy et al. 2021), unless otherwise noted. The mask basically consists of all voxels with  $S/N > 4$  over two successive velocity channels and then expanded to the contiguous voxels with  $S/N > 2$ . The “strict” moment maps are characterized to have high confidence but exclude faint structures, i.e., have lower completeness.

## 3. Results

We show the 55 pc resolution [C I](1–0) and CO(1–0) integrated intensity maps toward the central 1 kpc of NGC 1068 in Figures 1(a)–(b). As observed in many other galaxies (e.g., Miyamoto et al. 2021 and references therein), [C I](1–0) basically traces structures seen in CO(1–0) (but see also Michiyama & Ueda 2020 for an exceptional case).

However, if we focus on the projected area of the biconical ionized gas outflow (e.g., Das et al. 2006, hereafter D06), whose outline is highlighted by two dashed lines, the [C I] distribution is more extended than CO.

### 3.1. [C I] versus CO at 55 pc Scale

In order to quantify the apparent differences, we compare the two maps on a pixel-by-pixel basis (Figures 1(c)–(d)). The log–log scatter plot and the [C I]/CO line-ratio map show three characteristic features:

1. *Highest ratios:* Pixels coinciding with the biconical ionized gas outflow (FoV-1; colored points in Figure 1(d)) show [C I] emission comparably bright to CO in Kelvin units. The highest ratios are located 200–300 pc away from the AGN position (Figure 1(c)), which is beyond the outer radius of the CND ( $r_{\text{out}} \simeq 200$  pc; e.g., García-Burillo et al. 2014). The 5th–16th–50th–84th–95th percentiles of the ratio distribution are 0.16–0.33–0.72–1.86–4.86.
2. *Moderate ratios:* Pixels not affected by the ionized gas outflow in FoV-1 (black points) show moderately high line ratios. The percentiles are 0.12–0.22–0.39–0.62–0.86. This is similar to the [C I]/CO line ratio of 0.5–0.9 toward the AGN position of the Seyfert galaxy NGC 7469 (Izumi et al. 2020). In NGC 7469, the highest line ratio is found in the vicinity of the AGN position at 100 pc resolution. This is quite different from the NGC 1068 case, where line ratios ( $> 0.5$ ) are high almost everywhere in the central kiloparsec region, and the highest ratio is outside the CND.
3. *Low ratios:* The scatter plot shows a superlinear relation for the starburst ring (FoV-2 and FoV-3; gray points). In stark contrast to FoV-1, almost all the data points show  $[C I]/CO < 0.5$ . The five percentiles are 0.04–0.08–0.15–0.23–0.45. The superlinear [C I]–CO relation and the lower ratio are common features found in nearby starburst galaxies and their nuclei (e.g., Jiao et al. 2019; Salak et al. 2019; Saito et al. 2020).

Further investigation of the different [C I] properties among FoV-1, FoV-2, and FoV-3 is beyond the scope of this dedicated outflow study and will be discussed in a forthcoming paper. We note that we applied the same scatter analysis to the data cubes before collapsing and found exactly the same trend as described above.

### 3.2. The Kinematics of the High-[C I]/CO-ratio Gas

The [C I]/CO integrated intensity ratio map shows unusual line ratio values as described above, although this is not enough to fully uncover the characteristics of the [C I]/CO line ratio in NGC 1068. In this section, we try to constrain the geometry and kinematics of the high-ratio gas.

In Figure 2(a), we show channel maps of the [C I]/CO intensity ratio within FoV-1. Each datacube is rebinned to  $2.38 \text{ km s}^{-1}$  spectral resolution before calculating the ratio. Then, the systemic velocity of NGC 1068 ( $v_{\text{sys}} = 1116 \text{ km s}^{-1}$ ; García-Burillo et al. 2014) is subtracted. Here we follow the radio velocity convention with the kinematic LSR frame. In these channel maps, in addition to the pixels detected in both

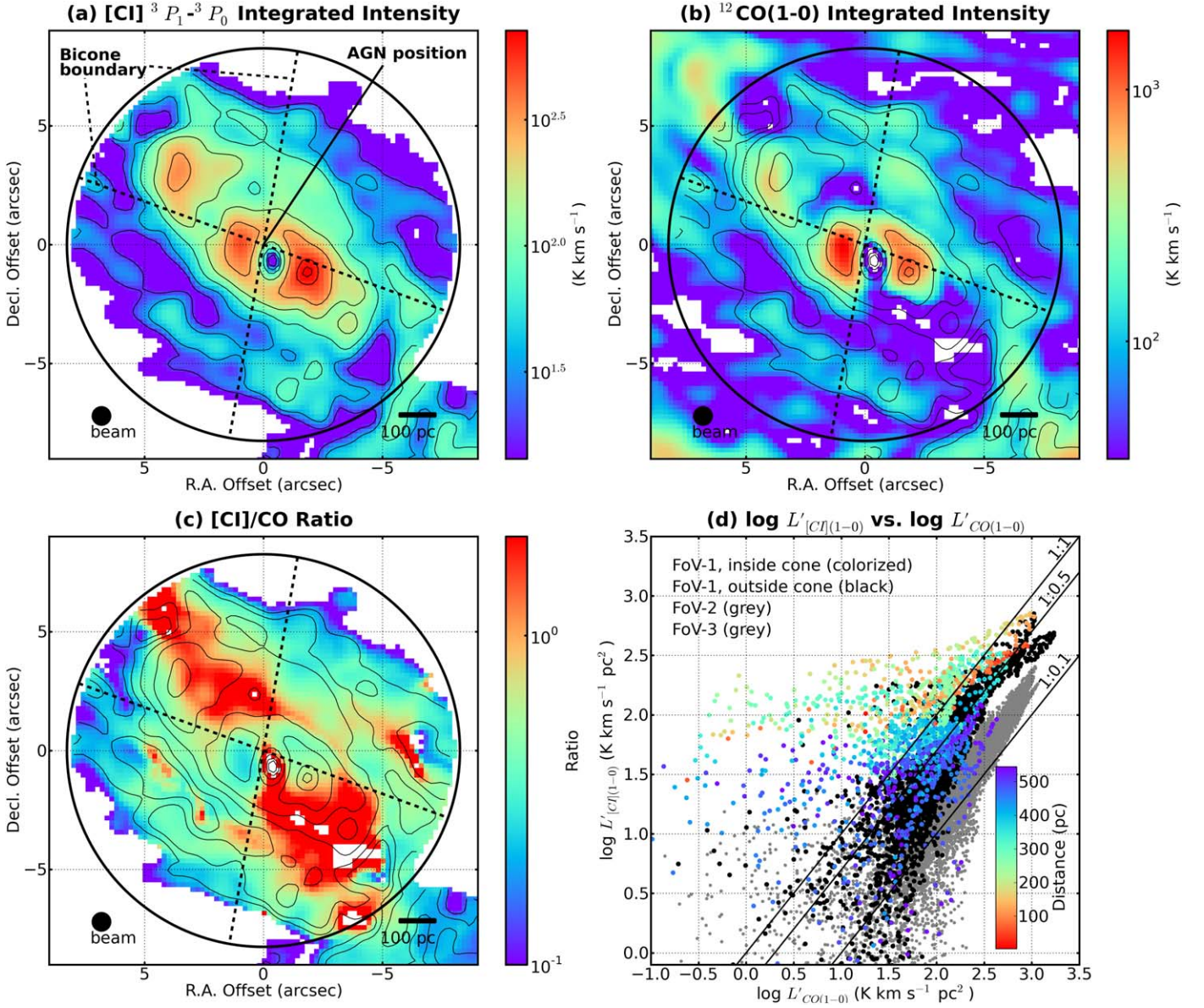


**Figure 1.** (a) [C I](1–0) integrated intensity map of the central 1 kpc of NGC 1068 (FoV-1) at  $0''.8$  resolution ( $\sim 55$  pc). The contours are  $(0.025, 0.05, 0.1, 0.2, 0.4, 0.8, \text{ and } 0.96) \times \text{peak}$ , where peak =  $714 \text{ K km s}^{-1}$ . The two dashed lines crossing the AGN position (Roy et al. 1998) denote the approximate outer edges of the ionized gas cones (Mingozzi et al. 2019). The black circle indicates the FoV of the Band 8  $12 \text{ m} + 7 \text{ m}$  data. (b) CO(1–0) integrated intensity map at  $0''.8$  resolution (T. Tosaki et al., in preparation). The [C I](1–0) contours are overlaid. (c) [C I](1–0)/CO(1–0) integrated intensity ratio map. (d) Pixel-by-pixel comparison between the [C I](1–0) and CO(1–0) maps. Pixel size is  $0''.2 \times 0''.2$ . Pixels within the cones in FoV-1 are colorized by their projected distance from the AGN position, and pixels outside the cones in FoV-1 are shown in black. Pixels in FoV-2 and FoV-3 (two positions in the starburst ring; Takano et al. in preparation) are shown in gray for reference.

the [C I] and CO lines, we show pixels with significant [C I] detection but CO nondetection in the reddest color (i.e., pixels with a ratio higher than unity).

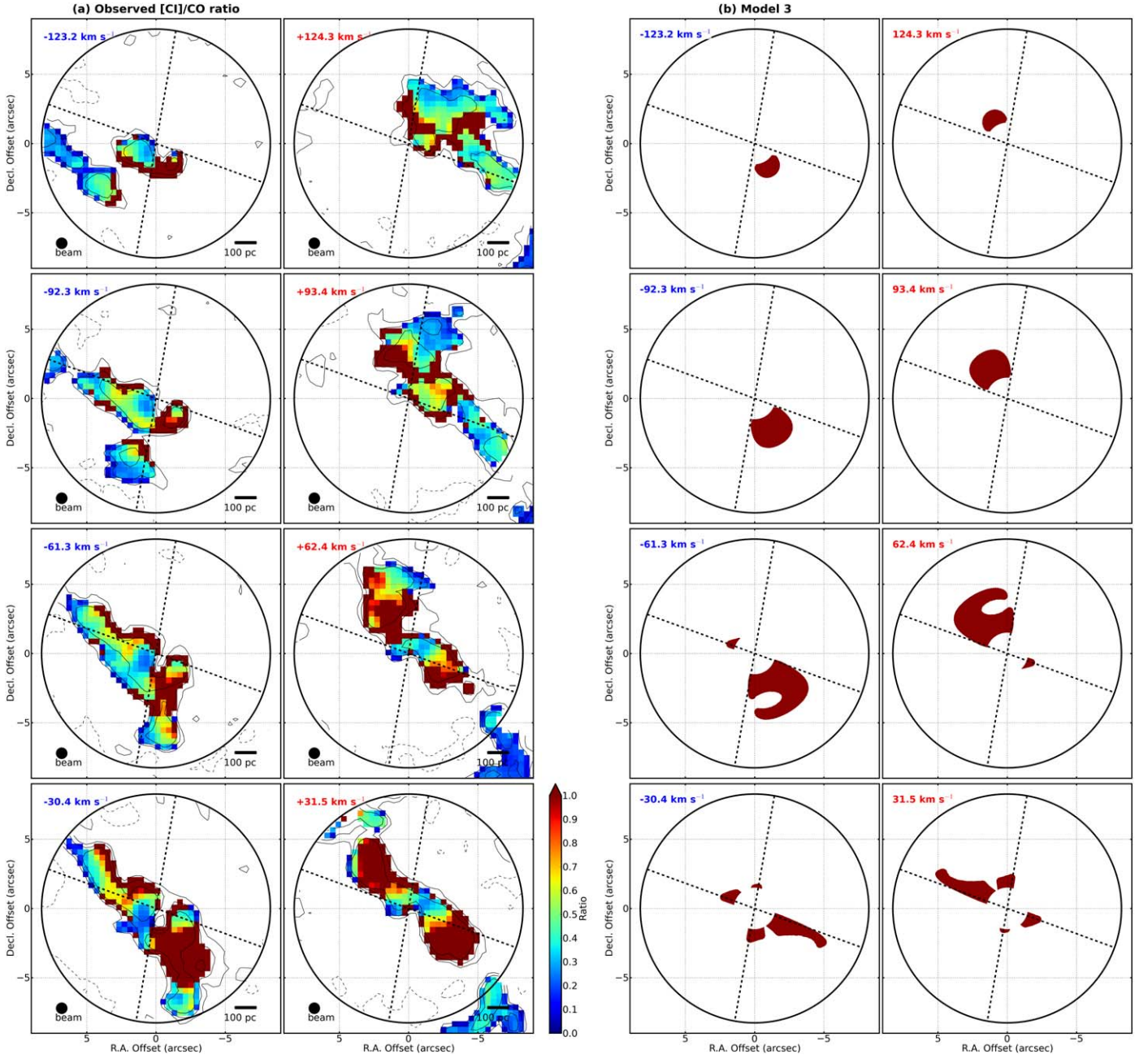
In each channel, the highest-ratio gas shows the same trend as seen in the integrated intensity ratio map (see Section 3.1), i.e., the highest-ratio pixels ( $>1$ ) preferentially appear within the ionized gas bicone whereas moderate ratios are outside the bicone. The highest-ratio gas shows a systematic velocity structure with extended, low-velocity components ( $|v - v_{\text{sys}}| \lesssim 65 \text{ km s}^{-1}$ ) and compact, high-velocity components ( $\gtrsim 80 \text{ km s}^{-1}$ ). This systematic motion seems to deviate from the nearly east–west velocity gradient due to galactic rotation, which is well traced in the low-ratio gas (green to blue pixels in

Figure 2(a); see Schinnerer et al. 2000 for a detailed modeling of the disk kinematics).

### 3.3. Modeling the Channel Map

Motivated by the properties of the [C I] line described above and the similarity between the high-ratio gas distribution and the projected distribution of the ionized gas bicone, here we compare the observed channel map with channel maps reproduced from simple bicone models.

In order to create model channel maps, we follow the bicone modeling method described in D06. They reproduced the results of multiple long-slit observations of the [O III] line around the center of NGC 1068 using a simple bicone model, which is widely accepted and consistent with the results based



**Figure 2.** (a) [C I]/CO intensity ratio channel maps of NGC 1068. We show pixels with a lower limit of the ratio higher than unity in the reddest color (i.e., CO non-detected pixels but detected in [C I]). The left (right) panels show the blueshifted (redshifted) part from the systemic velocity. The relative velocity offset is larger in the upper panels. The [C I] contours are overlaid. (b) Channel maps of the truncated, decelerating bicone model. This simple model largely reproduces the kinematics of the observed high-ratio gas shown in red.

on different methods and different data sets (e.g., Barbosa et al. 2014).

The position angle, (outer) opening angle, and inclination of our bicone model are exactly the same as in the D06 model, i.e.,  $30^\circ$ ,  $40^\circ$ , and  $5^\circ$  ( $90^\circ$  for pole on), respectively. The bicone geometry on the sky is, in short, nearly face on, and the northeast cone is a bit closer. The maximum distance from the nucleus along the bicone axis is set to 400 pc as D06 did. This bicone has an inner opening angle of  $20^\circ$ , so that it is hollow but has a certain thickness defined by the outer and inner opening angles. After assigning a certain outflow velocity structure to the bicone, we calculate, for each element composing the bicone in  $xyz$  space, its projected position and

velocity on the sky. From this projected model we extract channel maps matching our data. After convolving the model with a  $0''.8$  beam, we mask the central  $4''.0$  diameter as the observed data are severely affected by the CND. Because the [O III] outflow velocity assigned to the D06 model (intrinsic velocity  $v_{\text{int}} \lesssim 2000 \text{ km s}^{-1}$  and projected velocity  $v_{\text{proj}} \lesssim 1000 \text{ km s}^{-1}$ ) is much faster than the observed  $v_{\text{proj}}$  of the [C I] outflow ( $\lesssim 150 \text{ km s}^{-1}$ ; Figure 2(a)), we explore the velocity structure of the [C I](1–0) outflow using three different models.

After careful exploration of the three models, we conclude that only the third model can well reproduce the observed

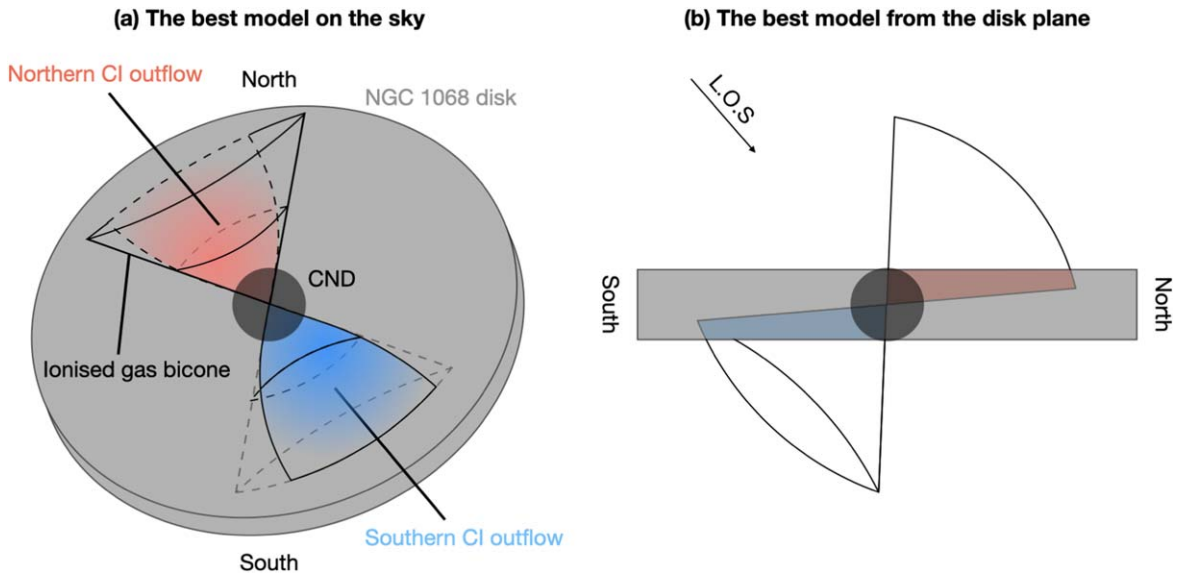


**Figure 3.** Illustrations of the truncated, decelerating bicone model (model 3). (a) View from Earth. (b) View from the disk plane. The high-[C I]/CO-ratio gas is distributed within the red and blue parts (i.e., overlap regions between the bicone and the disk).

kinematics of the high-[C I]/CO-ratio gas. Here we briefly explain the three bicone models:

1. *Model 1:* We start from a bicone model with a constant outflow velocity ( $v_{\text{int}} = 300 \text{ km s}^{-1}$ ) as shown in Figure 4(a) in Appendix A. The nearly face-on geometry and the wide opening angle naturally result in the bicone shape in both the blue- and redshifted channels. The two striking failures of this model are (A) the presence of extended high-velocity components and (B) the presence of northern blueshifted and southern redshifted components, both of which are not seen in the real data. Note that varying  $v_{\text{int}}$  does not improve this model in terms of these aspects.
2. *Model 2:* In order to achieve compact distributions in high-velocity channels (failure A), we introduce a varying velocity structure to model 1. D06 required deceleration after acceleration in order to explain the [O III] observations. To do so, they introduced a turnover radius,  $r_t$ , 140 pc away from the nucleus. The outflow velocity peaks at  $r_t$ . We simply employ this. However, as  $r_t$  is comparable to the CND size, the accelerating part is masked in our model channel maps. Therefore, we only model the decelerating part. We define  $v_{\text{int}}(r) = v_{\text{max}} - k(r - r_t)$ , where  $v_{\text{max}}$  is the maximum velocity of  $300 \text{ km s}^{-1}$ ,  $k$  is  $v_{\text{max}}/3r_t$ , and  $r$  is the distance from the nucleus ( $v_{\text{int}}$  reaches  $0 \text{ km s}^{-1}$  at  $r = 4r_t$ ). The model channel maps are shown in Figure 4(b) in Appendix A. As intended, model 2 reproduced the compact distributions in high-velocity channels. However, failure B of model 1 is still visible and could not be solved with any choice of  $k$  and  $v_{\text{max}}$ .
3. *Model 3:* After some exercises with models 1 and 2, we come to the conclusion that a “perfect” bicone geometry can never reproduce the observed channel map (failure B) because the nearly face-on geometry and the wide opening angle should always give both the blue- and redshifted components to both the northern and southern cones regardless of the velocity structure. More specifically, the foreground part (= blueshifted) of the northern

cone and the background (= redshifted) part of the southern cone are not visible in the real data.

Recalling the D06 model, one important information that our models 1 and 2 are missing is the possible interaction with the galactic molecular gas disk. This is also clearly seen in the schematic illustration provided by García-Burillo et al. (2019). This interaction is actually expected considering the geometry of the nearly face-on bicone ( $i = 5^\circ$ ) and the relatively face-on galactic molecular gas disk ( $i = 41^\circ$ ; Schinnerer et al. 2000; García-Burillo et al. 2014). Here we reproduce the “imperfect” (or truncated) bicone geometry based on the assumption that high-[C I]/CO line ratio gas is arising from regions where the bicone overlaps with the galaxy disk in  $xyz$  space. We assume a constant height of the molecular gas disk of 150 pc, a disk position angle of  $278^\circ$ , and a disk inclination of  $41^\circ$ . The disk thickness is consistent with the scale heights measured for nearby spiral galaxies (50–200 pc; Patra 2019). The resultant channel maps are shown in Figure 2(b). Although some substructures in the low-velocity channels are not exactly recovered (which are likely due to the contribution from galaxy rotation and the presence of the bar), the overall trend seen in the high-velocity channels of the real data is well reproduced.

Model 3 best reproduces the observed channel maps of the high-[C I]/CO-ratio gas with only three assumptions: (1) a bicone geometry exactly matching the known ionized gas bicone, (2) a decelerating velocity structure at  $r > r_t$ , and (3) an interaction with the galaxy disk (see Figure 3 for illustrations of the orientation). We assumed the geometry employed by the D06 [O III] outflow model; interestingly, the spatial configuration of model 3 is consistent with the molecular outflow model described by García-Burillo et al. (2014, 2019). This implies that the [O III], [C I], and CO outflows are closely related to each other.

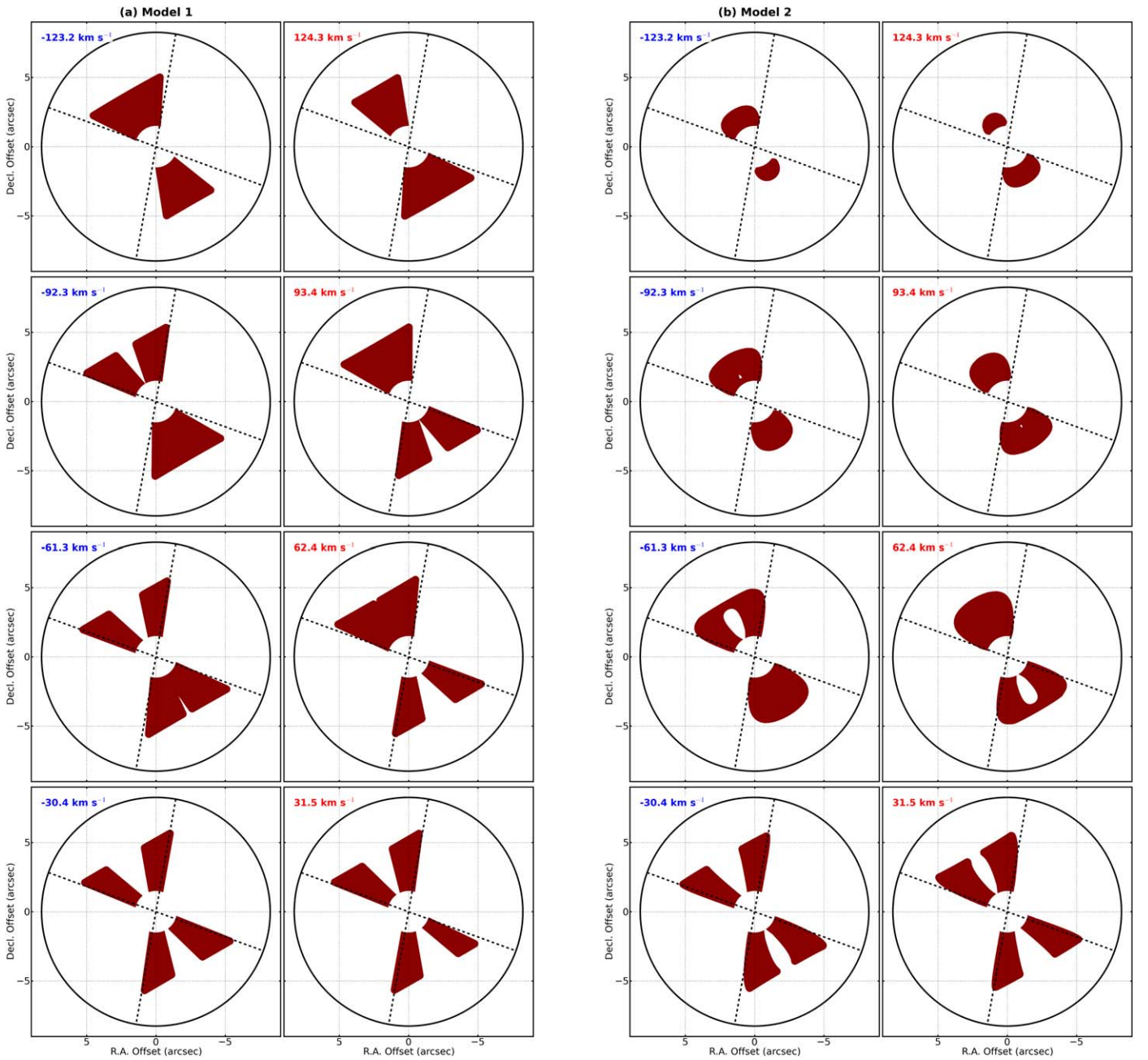


**Figure 4.** (a) The constant bicone model with no truncation (model 1). (b) The decelerating bicone model with no truncation (model 2).

### 3.4. The [C I] Bicone Model in Comparison with Observations and Simulations

In the previous section, we found that the spatial distribution of the high-[C I]/CO-ratio gas ( $>1$ ) in NGC 1068 can be simply explained by the interaction between the hundred-parsec-scale biconical outflow of the ionized gas (e.g., D06) and the molecular gas disk. Here we briefly discuss how this [C I] picture fits in with previous observational and theoretical studies.

Many previous observational studies revealed that there is a tight spatial correlation between the AGN narrow-line region (e.g., D06; Mingozzi et al. 2019), the radio jet (e.g., Gallimore et al. 1996; Capetti et al. 1997), and the entrained molecular gas in NGC 1068 (e.g., Krips et al. 2011; García-Burillo et al. 2014) from a few tens of parsecs up to  $\sim 500$  pc, all implying

that the outflow and the jet in NGC 1068 (1) are driven by the central AGN and (2) interact with the CNB and the galactic molecular gas disk (see also Barbosa et al. 2014). Although the exact cause for the hundred-parsec-scale ionized gas outflow is still under debate (e.g., see May & Steiner 2017), many models agree that the jet from the AGN (and its interaction with the multiphase ISM in the disk) is the origin of all the outflow phenomena in NGC 1068.

This jet–ISM interaction is observationally and theoretically known to produce an expanding energy bubble. This heats the surrounding medium and creates shocks at the colliding interface resulting in radial multiphase outflows (e.g., Matsushita et al. 2007; Sutherland & Bicknell 2007; Nesvadba et al. 2008; Wagner & Bicknell 2011; Wagner et al. 2012; Morganti et al. 2015). Mukherjee et al. (2016) suggested that weak radio jets (radio power  $\lesssim 10^{43}$  erg s $^{-1}$ ) are less efficient in

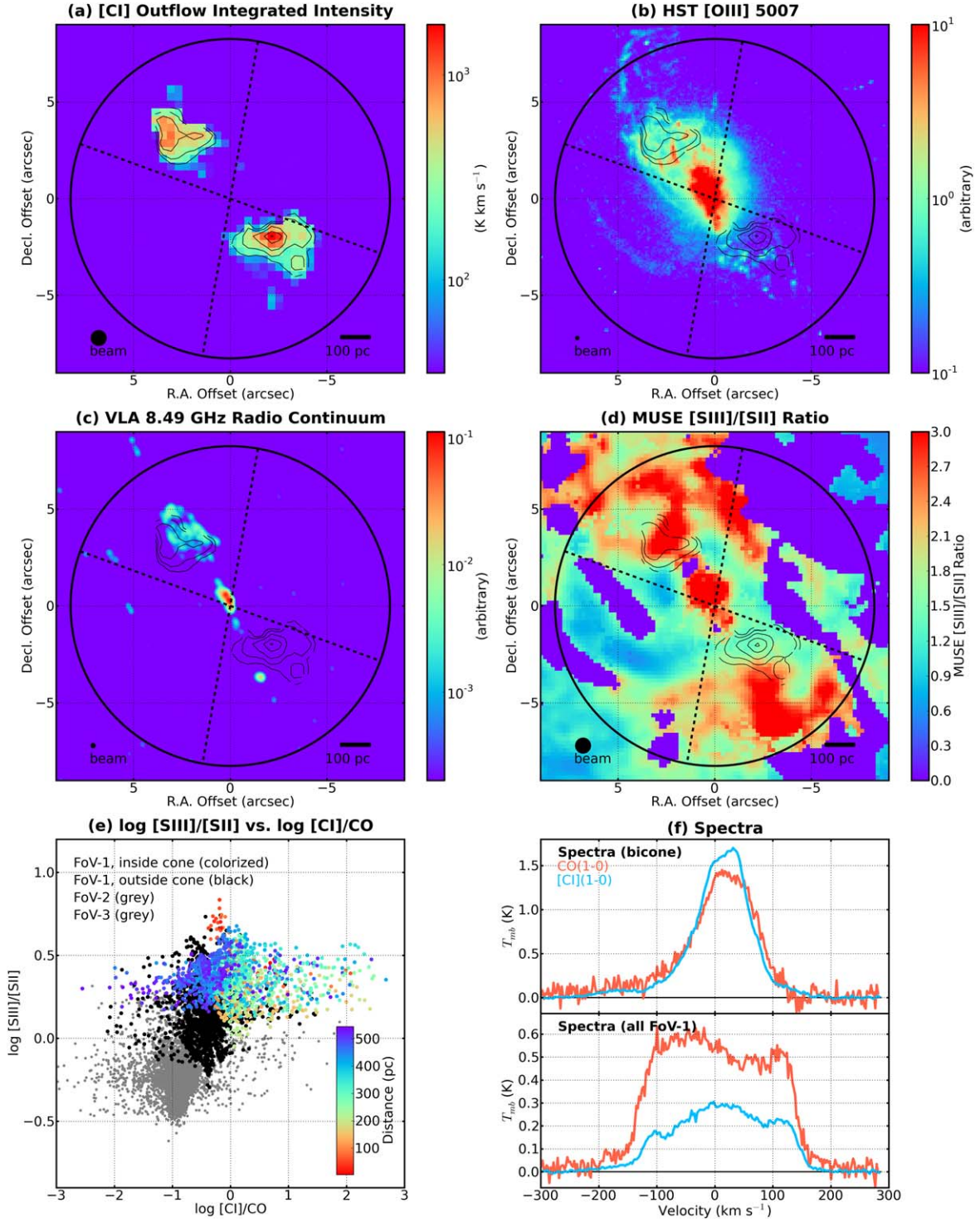


**Figure 5.** (a) The [C I] outflow intensity map (see Appendix B). (b) HST [O III] map. (c) VLA 8.49 GHz radio continuum map. (d) VLT/MUSE [S III]/[S II] line ratio map (i.e., ionization parameter map). (e) Pixel-by-pixel comparison between the [C I](1–0)/CO(1–0) ratio and [S III]/[S II] ratio maps. Pixels within the cones in FoV-1 are color-coded by projected distance from the AGN, and pixels lying outside the cones in FoV-1 are shown in black. Pixels in FoV-2 and FoV-3 (i.e., starburst ring) are shown in gray. (f) [C I](1–0) and CO(1–0) spectra toward the bicone (top) and FoV-1 (bottom). We use the [C I]-detected pixels of Figure 5(a) when extracting the bicone spectra.

accelerating and sweeping clouds but are able to affect the ISM over a large volume (especially in the lateral direction) because weak jets are trapped by the ISM for a long time. This “weak” radio jet scenario is consistent with the estimated radio power of NGC 1068 ( $1.8 \times 10^{43}$  erg s<sup>-1</sup>; García-Burillo et al. 2014).

The low [C I] outflow velocity in our model ( $v_{\max} = 300$  km s<sup>-1</sup>) compared to the ionized gas outflow velocity ( $v_{\max} = 2000$  km s<sup>-1</sup>; D06) supports the idea that shocks propagating from the weak jet are insufficient to accelerate molecular clouds in the disk but do efficiently heat the ISM as suggested by Mukherjee et al. (2016).

The shocks propagating through the dense gas heat, dissociate, and ionize the gas. The subsequent emission also produces ionizing and dissociating photons. We expect that those destructive processes, shock, dissociation, and ionization, happen in the overlap region between the outflow and the disk at the same time. Here we briefly discuss two possible mechanisms enhancing [C I]: shock dissociation and photodissociation.

In the shocked gas, H atoms (shock products of efficient H<sub>2</sub> destruction) endothermically dissociate CO and produce C atoms (e.g., Hollenbach & McKee 1980). Hollenbach & McKee (1980) also mentioned that the detection of high-speed interstellar molecules indicate that molecular gas re-formed in the postshock gas. However, if the re-formation process dominates in the outflow, the [C I]/CO ratio should return to the original value. We take  $\sim 0.2$  as observed in FoV-2 and FoV-3 to be representative for gas not affected by the outflow. Thus, although we expect that both shock dissociation and re-formation happen in the postshock gas, dissociation has to overwhelm re-formation in order to explain the observed high [C I]/CO ratio. In addition, as suggested by García-Burillo et al. (2017), the enhancement of C<sub>2</sub>H in the molecular outflow of NGC 1068 is likely due to the jet-driven dissociation and short lived ( $\sim 10^2$ - $10^3$  yr<sup>-1</sup>), implying that short-lived dissociation is an ongoing, continuous process in the outflow.

Similar to the shock dissociation as described above, when clouds are irradiated by a strong UV field, CO column density decreases and C column density increases (Meijerink & Spaans 2005). Meijerink & Spaans (2005) also predicted an enhancement of C atoms due to X-rays. All those processes likely result in higher [C I]/CO intensity ratios. The presence of kiloparsec-scale hot outflows in X-ray and FUV (e.g., Ogle et al. 2003) observationally supports this picture. However, based on the current data and analysis, we cannot rule out that UV and X-ray photons coming from the AGN play an important role in the molecular gas dissociation/ionization in the overlap region.

Combining our [C I] study with multiwavelength observations (Figures 5(a)–(d)) and simulations, we suggest that the highly inclined jet (radiatively and mechanically) heats, dissociates, and ionizes the ISM in the central kiloparsec of the disk (i.e., neutral gas clouds are not launched from the AGN). Thus, the AGN jet feedback suppresses “future” star formation in this part of the disk by destroying molecular clouds, not by efficiently sweeping them. A part of the phenomenon is observed as a strong pixel-by-pixel correlation between our [C I]/CO-ratio map (i.e., molecular cloud dissociation) and the [S III]/[S II] ratio map (i.e., high ionization; Mingozzi et al. 2019) at 55 pc resolution (Pearson correlation coefficient  $r = 0.62$ ; see Figure 5(e)).

One could consider that strong UV radiation from young massive stars forming in the clouds entrained in the outflow can explain the observed high [C I]/CO ratio, i.e., positive-feedback scenario. However, taking the  $v_{\text{int}}$  ( $\sim 2000$  K km s<sup>-1</sup>) and the maximum distance from the nucleus ( $\sim 400$  pc) of the ionized gas outflow (D06), the timescale of the outflow phenomenon is just  $\sim 0.2$  Myr. As this is too short to allow the clouds to form stars (typical star formation timescale is 30 Myr; e.g., Kawamura et al. 2009), we deem the positive-feedback scenario unlikely.

We note that there is an alternative way to realize multiphase outflows, which is an “in situ cold gas formation” scenario

(e.g., see Girichidis et al. 2021 and references therein). However, this prefers a “perfect” bicone geometry for the cold gas outflow as gas cooling isotropically happens, which is inconsistent with the observed truncated bicone. In addition, the efficient cooling may result in CO enhancement, not only of C, which is unlikely the case of NGC 1068, as the CO map shows holes toward the bicone direction (Figure 1(b)).

#### 4. Summary and Implications

In this Letter, we present high-resolution (0''8) ALMA observations of [C I](1–0) and CO(1–0) toward the central 1 kpc of the Type 2 Seyfert galaxy NGC 1068. We found a kiloparsec-scale elongated structure with an extremely high [C I]/CO intensity ratio ( $>1$ ), which coincides well with the spatial distribution of the known biconical ionized gas outflow. Our simple kinematic modeling, combined with multiwavelength studies in the literature, shows that the high-ratio gas is likely due to the interaction of the jet/ionized gas outflow with the galaxy disk. This interaction results in efficient dissociation (high [C I]/CO ratio) of molecular clouds within the disk plane. Thus, this is clear evidence for the negative AGN feedback in the central 1 kpc of NGC 1068. We suggest that the relatively weak radio jet results in large-scale molecular gas dissociation, which is more efficient than the sweeping effect at this stage.

Our current analysis is based on line intensities. This makes it difficult to constrain the physical and chemical properties of the negative AGN feedback happening in NGC 1068 by direct comparison with models. Thus, an accurate measurement of the [C I] column density by observing the other [C I] transition represents a future direction.

This work was supported by NAOJ ALMA Scientific Research grant No. 2021-18A. N.H. acknowledges support from JSPS KAKENHI grant No. JP21K03634. E.H. acknowledges support from the US National Science Foundation, grant 19-06489. K.K. acknowledges support from JSPS KAKENHI grant No. JP17H06130. The work of Y.N. was supported by NAOJ ALMA Scientific Research grant No. 2017-06B and JSPS KAKENHI grant Number JP18K13577. T.T. acknowledges support from JSPS KAKENHI grant No. JP20H00172. This paper makes use of the following ALMA data: ADS/JAO.ALMA#2017.1.00586.S and ADS/JAO.ALMA#2018.1.01684.S. ALMA is a partnership of ESO (representing its member states), NSF (USA) and NINS (Japan), together with NRC (Canada), MOST and ASIAA (Taiwan), and KASI (Republic of Korea), in cooperation with the Republic of Chile. The Joint ALMA Observatory is operated by ESO, AUI/NRAO and NAOJ. This research has made use of the NASA/IPAC Extragalactic Database (NED), which is funded by the National Aeronautics and Space Administration and operated by the California Institute of Technology. The National Radio Astronomy Observatory is a facility of the National Science Foundation operated under cooperative agreement by Associated Universities, Inc. This research has made use of the SIMBAD database, operated at CDS, Strasbourg, France. Data analysis was in part carried out on the Multi-wavelength Data Analysis System operated by the Astronomy Data Center (ADC), National Astronomical Observatory of Japan.

*Software:* ALMA Calibration Pipeline, Astropy (Astropy Collaboration et al. 2013, 2018), CASA (McMullin et al. 2007), NumPy (Harris et al. 2020), PHANGS-ALMA

Pipeline (Leroy et al. 2021), SciPy (Virtanen et al. 2020), spectral-cube (Ginsburg et al. 2019), radio-beam.

### Appendix A Three Biconical Outflow Models

In Figure 4, we show the two models (models 1 and 2) that do not reproduce the observed characteristics of the high-[C I]/CO-ratio gas in the central region of NGC 1068 (see Section 3.3). The observed channel maps and the channel maps of model 3 are shown in Figure 2.

### Appendix B Multiwavelength View of the Outflow and the Jet

For comparison with our ALMA maps, we downloaded the MUSE [S III] $\lambda\lambda$  9069,9532/[S II] $\lambda\lambda$  6717,6731 ratio map,<sup>13</sup> proxy for the metallicity-independent ionization parameter (see Mingozzi et al. 2019 for a detailed description). In addition, the 8.49 GHz radio continuum map taken by the Karl G. Jansky Very Large Array (VLA) is retrieved from the VLA Data Archive.<sup>14</sup> We also downloaded drizzled HST WFPC2 F502N and F547M maps from the Hubble Legacy Archive<sup>15</sup> in order to create an [O III] $\lambda\lambda$ 5007 map. Both the VLA and HST maps have a higher angular resolution and image a larger area than the [C I](1–0) map.

In Figures 5(b)–(d), those three ancillary maps are shown, as well as our [C I] map for comparison. The [C I] outflow intensity map (Figure 5(a)) is created as follows: (1) create a mask cube using the line ratio cube (Figure 2(a)) clipped at ratio >1, (2) apply the mask to the [C I] datacube, and then (3) collapse it. We note that the [C I] intensity map shown in Figure 1(a) is created without this line ratio mask.

In Figure 5(e), we show a pixel-by-pixel comparison between the [S III]/[S II] ratio and [C I]/CO-ratio maps in the same manner as Figure 1(d). Data points within the bicone of FoV-1 show systematically higher ratio values compared to the data from FoV-2 and FoV-3 (i.e., starburst ring), implying that normal star-forming activities happening in NGC 1068 cannot explain the observed values within the bicone.

We show averaged CO and [C I] spectra in Figure 5(f). As, in general, molecular outflow studies focus on line profiles, it is important to check how the [C I] outflow spectrum looks. To make outflow spectra, we employ a fine-tuned version of the method described in Stuber et al. (2021), i.e., extracting outflow spectra based on a mask and comparing it with a galaxy-averaged spectrum.

### Appendix C Derived Parameters of the Cold Gas Outflow

Here we briefly summarize the parameters of the best bicone model (i.e., model 3) for the [C I] outflow. As we basically applied the D06 model that well describes the [O III] outflow of NGC 1068, we use the same symbols as defined in D06.

The maximum distance along the bicone axis from the nucleus  $z_{\max}$  is 400 pc, the inner opening angle of the bicone  $\theta_{\text{inner}}$  is 20°, the outer opening angle  $\theta_{\text{outer}}$  is 40°, the inclination angle between the bicone axis and the plane of the sky  $i_{\text{axis}}$  is

5°, and the position angle  $\text{PA}_{\text{axis}}$  is 30°. These values are exactly the same as the D06 model, and we did not need to modify these parameters to explain the [C I] and CO data. However, we need a more sophisticated model to constrain them.

We also assumed the velocity structure employed by the D06 model, i.e.,  $v_{\text{int}}(r) = v_{\text{max}} - k(r - r_i)$  (see Section 3.3). This decelerating model is required to explain the observed characteristics of the [C I] and CO outflows, although the maximum velocity of the [O III] outflow ( $v_{\text{max}} \sim 2000 \text{ km s}^{-1}$ ) is too fast. After some exploration of the parameter space from 100 to 2000  $\text{km s}^{-1}$ , we found that  $v_{\text{max}} \sim 300 \text{ km s}^{-1}$  can reproduce the observed [C I] and CO channel maps.

We suggest that the bright [C I] emission comes from the region where the ionized gas outflow hits the galactic disk in order to explain the “imperfect” bicone geometry. We employed the disk model described in Schinnerer et al. (2000). This spatial configuration is consistent with the model described in García-Burillo et al. (2014, 2019). Based on the configuration, there are two regions (north and south) where [C I] emission is enhanced as shown in Figure 5(a). The measured [C I] luminosity and CO luminosity of the northern outflow are  $10^{5.37} \text{ K km s}^{-1} \text{ pc}^2$  and  $10^{5.33} \text{ K km s}^{-1} \text{ pc}^2$ , and the luminosities of the southern outflow are  $10^{5.41} \text{ K km s}^{-1} \text{ pc}^2$  and  $10^{5.25} \text{ K km s}^{-1} \text{ pc}^2$ , respectively. Although measuring molecular gas masses is important to characterize the cold gas outflow of this galaxy, it requires additional data sets and efforts (e.g., need a gold standard gas mass tracer). This is an interesting topic for future projects.

### ORCID iDs

Toshiki Saito  <https://orcid.org/0000-0002-2501-9328>  
 Shuro Takano  <https://orcid.org/0000-0001-6788-7230>  
 Nanase Harada  <https://orcid.org/0000-0002-6824-6627>  
 Taku Nakajima  <https://orcid.org/0000-0002-8467-5691>  
 Eva Schinnerer  <https://orcid.org/0000-0002-3933-7677>  
 Daizhong Liu  <https://orcid.org/0000-0001-9773-7479>  
 Akio Taniguchi  <https://orcid.org/0000-0002-9695-6183>  
 Takuma Izumi  <https://orcid.org/0000-0001-9452-0813>  
 Kazuharu Bamba  <https://orcid.org/0000-0001-9720-8817>  
 Eric Herbst  <https://orcid.org/0000-0002-4649-2536>  
 Kotaro Kohno  <https://orcid.org/0000-0002-4052-2394>  
 Yuri Nishimura  <https://orcid.org/0000-0003-0563-067X>  
 Sophia Stuber  <https://orcid.org/0000-0002-9333-387X>  
 Yoichi Tamura  <https://orcid.org/0000-0003-4807-8117>  
 Tomoka Tosaki  <https://orcid.org/0000-0001-9016-2641>

### References

- Anand, G. S., Lee, J. C., Van Dyk, S. D., et al. 2021, *MNRAS*, 501, 3621  
 Astropy Collaboration, Robitaille, T. P., Tollerud, E. J., et al. 2013, *A&A*, 558, A33  
 Astropy Collaboration, Price-Whelan, A. M., Sipőcz, B. M., et al. 2018, *AJ*, 156, 123  
 Barbosa, F. K. B., Storchi-Bergmann, T., McGregor, P., Vale, T. B., & Rogemar Riffel, A. 2014, *MNRAS*, 445, 2353  
 Capetti, A., Axon, D. J., & Macchetto, F. D. 1997, *ApJ*, 487, 560  
 Costa, T., Sijacki, D., & Haehnelt, M. G. 2014, *MNRAS*, 444, 2355  
 Croft, S., van Breugel, W., de Vries, W., et al. 2006, *ApJ*, 647, 1040  
 Das, V., Crenshaw, D. M., Kraemer, S. B., & Deo, R. P. 2006, *AJ*, 132, 620  
 Gallimore, J. F., Baum, S. A., & O’Dea, C. P. 1996, *ApJ*, 464, 198  
 García-Burillo, S., Combes, F., Usero, A., et al. 2014, *A&A*, 567, A125  
 García-Burillo, S., Viti, S., Combes, F., et al. 2017, *A&A*, 608, A56  
 García-Burillo, S., Combes, F., Ramos Almeida, C., et al. 2019, *A&A*, 632, A61

<sup>13</sup> This is available at the CDS. See <http://cdsarc.u-strasbg.fr/viz-bin/qcat?J/A+A/622/A146>.

<sup>14</sup> <https://archive.nrao.edu/archive>

<sup>15</sup> <https://hla.stsci.edu/>

- Ginsburg, A., Koch, E., Robitaille, T., et al. 2019, radio-astro-tools/spectral-cube: Release v0.4.5, v0.4.5, Zenodo, doi:[10.5281/zenodo.3558614](https://doi.org/10.5281/zenodo.3558614)
- Girichidis, P., Naab, T., Walch, S., & Berlok, T. 2021, *MNRAS*, **505**, 1083
- Harris, C. R., Millman, K. J., van der Walt, S. J., et al. 2020, *Natur*, **585**, 357
- Hollenbach, D., & McKee, C. F. 1980, *ApJL*, **241**, L47
- Izumi, T., Nguyen, D. D., Imanishi, M., et al. 2020, *ApJ*, **898**, 75
- Jiao, Q., Zhao, Y., Lu, N., et al. 2019, *ApJ*, **880**, 133
- Kawamura, A., Mizuno, Y., Minamidani, T., et al. 2009, *ApJS*, **184**, 1
- Krips, M., Martín, S., Eckart, A., et al. 2011, *ApJ*, **736**, 37
- Leroy, A. K., Hughes, A., Liu, D., et al. 2021, *ApJS*, **255**, 19
- Magorrian, J., Tremaine, S., Richstone, D., et al. 1998, *AJ*, **115**, 2285
- Matsushita, S., Muller, S., & Lim, J. 2007, *A&A*, **468**, L49
- May, D., & Steiner, J. E. 2017, *MNRAS*, **469**, 994
- McMullin, J. P., Waters, B., Schiebel, D., Young, W., & Golap, K. 2007, in ASP Conf. Ser. 376, *Astronomical Data Analysis Software and Systems XV*, ed. R. A. Shaw, F. Hill, & D. J. Bell (San Francisco, CA: ASP), 127
- Meijerink, R., & Spaans, M. 2005, *A&A*, **436**, 397
- Michiyama, T., Ueda, J., Tadaki, K.-I., et al. 2020, *ApJL*, **897**, L19
- Mingozzi, M., Cresci, G., Venturi, G., et al. 2019, *A&A*, **622**, A146
- Miyamoto, Y., Yasuda, A., Watanabe, Y., et al. 2021, *PASJ*, **73**, 552
- Morganti, R., Oosterloo, T., Oonk, J. B. R., Frieswijk, W., & Tadhunter, C. 2015, *A&A*, **580**, A1
- Mukherjee, D., Bicknell, G. V., Sutherland, R., & Wagner, A. 2016, *MNRAS*, **461**, 967
- Nesvadba, N. P. H., Lehnert, M. D., De Breuck, C., Gilbert, A. M., & van Breugel, W. 2008, *A&A*, **491**, 407
- Ogle, P. M., Brookings, T., Canizares, C. R., Lee, J. C., & Marshall, H. L. 2003, *A&A*, **402**, 849
- Patra, N. N. 2019, *MNRAS*, **484**, 81
- Roy, A. L., Colbert, E. J. M., Wilson, A. S., & Ulvestad, J. S. 1998, *ApJ*, **504**, 147
- Saito, T., Michiyama, T., Liu, D., et al. 2020, *MNRAS*, **497**, 3591
- Salak, D., Nakai, N., Seta, M., & Miyamoto, Y. 2019, *ApJ*, **887**, 143
- Schinnerer, E., Eckart, A., Tacconi, L. J., Genzel, R., & Downes, D. 2000, *ApJ*, **533**, 850
- Silk, J. 2013, *ApJ*, **772**, 112
- Stuber, S. K., Saito, T., Schinnerer, E., et al. 2021, *A&A*, **653**, A172
- Sturm, E., González-Alfonso, E., Veilleux, S., et al. 2011, *ApJL*, **733**, L16
- Sutherland, R. S., & Bicknell, G. V. 2007, *ApJS*, **173**, 37
- van Breugel, W. J. M., & Dey, A. 1993, *ApJ*, **414**, 563
- Veilleux, S., Maiolino, R., Bolatto, A. D., & Aalto, S. 2020, *A&ARv*, **28**, 2
- Virtanen, P., Gommers, R., Oliphant, T., et al. 2020, *Nat. Methods*, **17**, 261
- Wagner, A. Y., & Bicknell, G. V. 2011, *ApJ*, **728**, 29
- Wagner, A. Y., Bicknell, G. V., & Umemura, M. 2012, *ApJ*, **757**, 136
- Wilson, A. S., & Ulvestad, J. S. 1983, *ApJ*, **275**, 8